Materials Research Proceedings 28 (2023) 31-40 https://doi.org/10.21741/9781644902479-4

Prediction of surface topography change during chain of selective laser melting and burnishing

TEIMOURI Reza[1,a *], SKOCZYPIEC Sebastian[1,b] and GRABOWSKI Marcin[1,c]

[1] Chair of Production Engineering, Department of Mechanical Engineering, Cracow University of Technology, Krakow, Poland

[a]reza.teimouri@pk.edu.pl, [b]sebastain.skoczypiec@pk.edu.pl, [c]marcin.grabowski@pk.edu.pl

Keywords: Surface Roughness, Selective Laser Melting, Burnishing, Simulation

Abstract. The present study developed theoretical models for simulation of surface topography and roughness of parts produced by the selective laser melting (SLM) process and their evolution after burnishing as post-treatment. The simulation algorithm has been integrated by combining principles of selective laser melting process, i.e., formation of the melt pool and kinematic of motion, followed by mechanic of burnishing through Z-map approach. To verify the simulation results, 316L stainless steel was 3D printed and then burnished under different burnishing depth. 3D surface profile and surface roughness of as-printed material and those post-processed by surface burnishing (SB) were measured through microscopic examination and surface roughness measurement, respectively. The results obtained through comparison of confirmatory experiments and simulation model affirmed that the proposed approach is accurate enough to predict the surface topography and roughness of as-printed and post-treated samples.

Introduction

Among various approaches for additive manufacturing (AM) of metallic material, selective laser melting (SLM) was significantly attractive to researchers and industries because of its ability to produce parts with complex geometries. However, due to the layer-upon-layer nature of production, the SLM suffers from a poor surface finish.

The post processing of AM samples by surface burnishing (SB) has some advantages over other mechanical surface treatment process. Compared to material-removal process [1-3], the burnishing causes surface sever plastic deformation and results in modification of surface and subsurface layers in terms of hardness, compressive residual stress and microstructure refining. On the other hand, compared to non-material removal process [4-6], burnishing results in superior surface finish. It has been reported that the surface finish of burnished samples can reach optical scale under optimum processing conditions [7]. On the other hand, further advantages of burnishing over the other non-material removal processes is its independency of complicated infrastructures such as ultrasonic apparatus or pneumatic units. The process can be implemented by a simple lathe or milling machine.

Recently, researchers have attracted it for the post-processing of metallic and non-metallic materials produced by AM. Rotella et al. [8] used ball burnishing for the post-processing of stainless steel GP1 produced by SLM. Sunny et al. [9] used interlayer roller burnishing as sequential to SLM to reduce the tensile residual stress of each built layer before addition of next one. Raaj et al. [10] applied SB for post-processing of Inconel 718 manufactured by electron beam additive manufacturing. Brujin et al. [11] stated that the SB is a suitable process for processing polymeric (fused filament fabricated) material produced by 3D printing. They stated that unlike to material removal-based surface finishing, burnishing doesn't change the chemical composition of samples because the temperature rise is limited.

The additive manufacturing chain that includes the SLM and post-processing must be designed and then optimized to a certain level to obtain the desired surface finish. In order to do so, the

Materials Research Proceedings 28 (2023) 31-40 https://doi.org/10.21741/9781644902479-4

developing an integrated simulation model which can predict the final surface finish in short period of the time will be more vital. Thus, in the present work, novel physics-based theoretical simulations are proposed to predict the surface roughness evolution of parts produced by SLM and post-processed by the surface burnishing process. Accordingly, the present work aims to simulate the 3D surface topography and roughness of parts made by SLM and then modified by the burnishing process.

Theoretical Simulation

The topography of the surface in the SLM process is generated through the formation of the solidified melt pool and duplication using kinematic motion. Thus, the shape of melt pool during the printing process must be modelled in the first step. Heat input from the laser power source is calculated using a point moving heat source solution that is successfully used for the SLM process [12]. The point moving heat source solution was derived from a general convection-diffusion equation, which can be expressed as:

$$\begin{cases} T - T_0 = \dfrac{P\eta}{4\pi kR}\exp\left(\dfrac{-V_L(R_T + y)}{2\kappa}\right) \\ \kappa = \dfrac{k}{\rho c} \\ R_T = \sqrt{x^2 + y^2 + z^2} \end{cases} \tag{1}$$

where T is the localized temperature, P is the laser power, η is the coefficient that determines how much of the laser heat source is absorbed by powder; κ is thermal diffusivity, R_T is the distance from the heat source location, V_L is the scan velocity during the printing process that is in y direction; k is the heat conduction coefficient, and ρ is the material density. Fig. 1a represents a schematic illustration of the cross section of melt pool and its geometrical characteristics of the SLM process. It is created by the distribution of temperature induced by moving laser heat sources. The cross-section of the melt pool in xz plane (as shown in Fig. 1a) determines the formation of a surface generation of the SLM process. During the printing process, the maximum melt pool depth can be calculated by substituting the melt temperature in Eq. 5 at the location of $x=0$, $y=0$ as shown in Fig. 1. Accordingly, the molten pool depth (d) is the absolute root of the following equation:

$$\begin{cases} \Delta d + \exp(\Theta d) = 0 \\ \Delta = 2\pi k\left(\dfrac{T_m - T_0}{P\eta}\right) \\ \Theta = \dfrac{V_L}{2\kappa} \end{cases} \tag{2}$$

where T_m is the melting temperature.

According to the reports of several researchers, the profile of the melt pool cross-section is a paraboloid [13]. Accordingly, the equation of cross section profile, the consumed powder bandwidth (W_0) and melt pool width (W) (as shown in Fig. 1b) are calculated by Eq. 3:

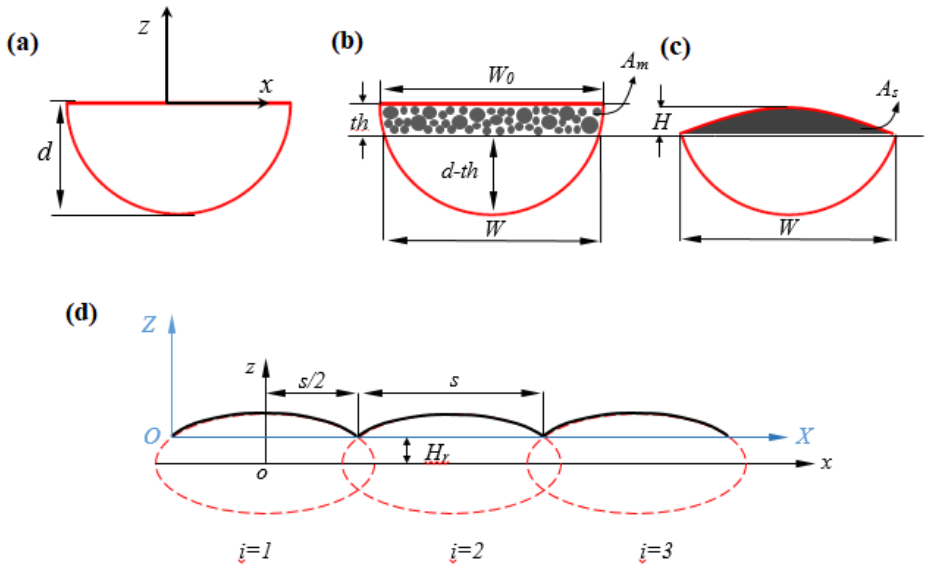

Fig. 1. (a) formation of cross section of melt pool (b) powder band width (c) solidified melt pool and formation of hump (d) generation of surface topography.

$$\begin{cases} z = x^2 - d \\ W_0 = 2\sqrt{d} \\ W = 2\sqrt{d - th} \end{cases} \tag{3}$$

where *th* is the layer thickness.

Once the melt pool is solidified, as a result of surface tension, a hump is formed on the upper side of the melt pool, as shown in Fig. 1c. Liu et al. [13] stated that the profile of the hump is a portion of an ellipse.

In order to calculate the maximum height of the hump area (that is usually called melt pool height), the mass conservation law is utilized. Accordingly, it is assumed that the mass of the region bounded by powder during melting is equal to the mass of the hump region after solidification. Hence, it can be said that the area of the region bounded by powder (i.e., A_m as shown in Fig. 1c) is equal to the hump area (i.e., A_s as demonstrated in Fig. 1e). Therefore, it can be written:

$$H = \frac{4}{W\pi}\left[Wth + 2\int_{\frac{W}{2}}^{\frac{W_0}{2}} \left(x^2 - d\right) dx \right] \tag{4}$$

By printing through a longitudinal direction, the melt pool with a fixed cross-section is lengthened to a predefined length. But, in the lateral direction, the cross sections of melt pools interact based on the hatch spacing value (s). Therefore, only a part of the ellipse contribution in the generation of surface topography, as shown in Fig. 1d. Accordingly, the surface generation equation can be:

$$Z = \left(\frac{2H}{W}\right)\left\{ \sqrt{W^2 - \left[X - (i-1)s\right]^2} - \sqrt{W^2 - \left(\frac{s}{2}\right)^2} \right\} \qquad (i-1)s < X < is \qquad i = 1, 2, \ldots N \tag{5}$$

The obtained 3D surface profile of the material after SLM is named H (X, Y, Z).

In order to model the evolution of SLM surface topography after burnishing, Z-map approach is being utilized that transforms the cloud of points from tool coordinate system to workpiece coordinate system through series of transformation matrix. Here the initial surface topography is the H (X, Y, Z) which is obtained for 3D printed material; this matrix will be updated by applying the Z-map transformative model [14]. According to the principle of Z-map model, different

reference frames on the roller, burnishing tool, machine tool, and workpiece were defined and presented in Fig. 3. Here the reference coordinate system O_W-$X_WY_WZ_W$ that is called the workpiece coordinate system. During the burnishing process, the O_W-$X_WY_WZ_W$ is fixed on the workpiece. The O_M-$X_MY_MZ_M$ is called machine coordinate system. Its origin is connected to the machine spindle. It has translational movement with respect to workpiece coordinate system (as shown in fig. 3a-3c). The tool coordinate system, O_M-$X_MY_MZ_M$ has similar origins to the machine coordinate system (Fig. 3b). It is transformed into a machine coordinate system through a rotational movement. The local coordinate system that is located on the roller is shown by O_K-$X_KY_KZ_K$. Depending to the number of rollers distributed on the circumference of the tool (as shown in Fig. 3d), the O_K-$X_KY_KZ_K$ is transformed to the tool coordinate system by a rotation considering the angle between each roller. Accordingly, the main formulation that transforms an individual point on the roller to workpiece coordinate system is:

$$\begin{bmatrix} X_P^W \\ Y_P^W \\ Z_P^W \\ 1 \end{bmatrix} = \begin{bmatrix} \cos\Phi_k & -\sin\Phi_k & 0 & 0 \\ \sin\Phi_k & \cos\Phi_k & 0 & 0 \\ 0 & 0 & 1 & 0 \\ 0 & 0 & 0 & 1 \end{bmatrix} \begin{bmatrix} \cos\omega t & \sin\omega t & 0 & 0 \\ -\sin\omega t & \cos\omega t & 0 & 0 \\ 0 & 0 & 1 & 0 \\ 0 & 0 & 0 & 1 \end{bmatrix} \begin{bmatrix} 0 & 0 & 0 & V_f t \\ 0 & 0 & 0 & 0 \\ 0 & 0 & 1 & R \\ 0 & 0 & 0 & 1 \end{bmatrix} \begin{bmatrix} X_P^K \\ Y_P^K \\ Z_P^K \\ 1 \end{bmatrix} \tag{6}$$

where Φ_k is angle between the k-th roller and tool axes that is function of initial phase and number of roller which can be calculated by Eq. 7. ω is the annular velocity that is $\omega = 2\pi N/60$. Also, V_f is the feed velocity.

$$\Phi_k = \frac{\Phi_0 + 2\pi(k-1)}{N_R} \tag{7}$$

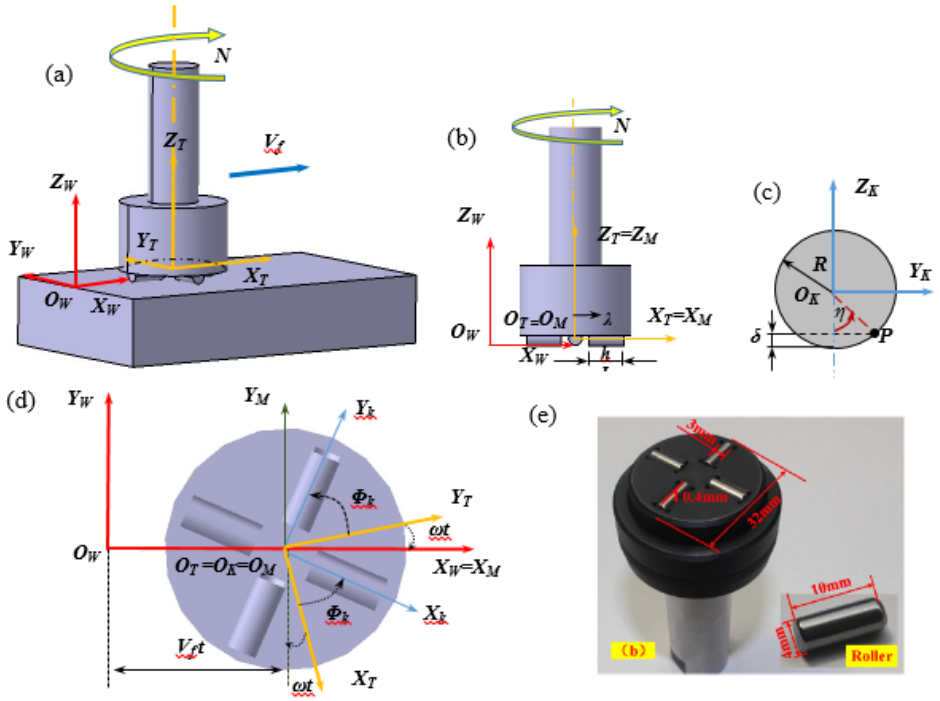

Fig. 2. (a) A schematic illustration of multi-roller rotary burnishing for flat surface including workpiece and tool coordinate systems (b) tool coordinate system (c) coordinate of an arbitrary point P on the roller with radius of r (d) trajectory of an obituary pint of P on different coordinate system i.e. roller, tool, machine and workpiece (e) real rotary burnishing tool with multi-roller.

In order to implement the algorithm, following steps need to be taken into consideration:
a) Initializing the burnishing process: burnishing parameters including the feed velocity (V_f), roller number (N_R), roller radius (R), depth of penetration (δ), and spindle speed (N) are set.
b) Discretization of workpiece surface: here, a slice of the workpiece with length of feed per revolution in X_W direction and width of $2R$ equal to the diameter of the burnishing tool in Y_W direction is considered. Here, the Z-map model of the workpiece with $m*n$ grids is established. The length and width of each grid are selected based on the gridding of the 3D printed surface in such a way that the hatch spacing is divided to 50 elements. Thus, the Δx equals $s/50$. Also, the width of each grid is selected as long as its length, i.e., $\Delta y=\Delta x$. Therefore, the selected region in X_W direction must be divided to:

$$\begin{cases} n_x = \dfrac{f}{\Delta x} \\ n_y = \dfrac{2R}{\Delta y} \end{cases} \tag{8}$$

c) Setting up the time increments: By identifying the processing length equal to f, it can be inferred that the process ends when this length is swept with burnishing tool. Therefore, the processing time can be obtained by dividing the burnishing feed rate i.e., f, by linear velocity i.e., V_f. Accordingly, the time increment (Δt) for processing the mesh length (Δx) with the same linear velocity is obtained by using the following formula:

$$\begin{cases} t = \dfrac{f}{V_f} = \dfrac{V_f \big/ N}{V_f} = \dfrac{1}{N} \\ \Delta t = \dfrac{\Delta x}{V_f} = \dfrac{1}{n_x N} \end{cases} \tag{9}$$

d) Discretization of the roller: Here it must be taken into consideration that the projection length of the roller element must be within the size of the workpiece's grid region. In other words, within each time increment, only one grid point of the workpiece is swept over by the discretized point of roller. In order to discretize the tool, couple considerations must be taken into account: (i) dividing the depth of penetration in different layers: based on the simulation's accuracy, the depth of penetration in axial direction (i.e. direction of Z_K) is divided into other parts and then the depth of each layer is δ_i (i=1, 2, …, n_i) will be $d\delta=\delta/n_i$; (ii) for each δ_i, there is a secant that causes variation of spreading angle. Their values can be calculated using the following equation:

$$\begin{cases} \eta_i = \cos^{-1}\left(\dfrac{R-\delta_i}{R}\right) \\ \delta_i = \dfrac{\delta_{\max}}{n_i} \end{cases} \tag{10}$$

Each layer must also be discretized based on dividing its corresponding spreading angle. Accordingly, the η_i is divided into n_j parts. Thus, each angular increment is calculated by:

$$\eta_{ij} = \frac{2\eta_i}{n_j} \quad j = 1,2,..,n_j \tag{11}$$

The value of n_j can be calculated arbitrary or based on interconnection with workpiece gridding using following equation:

$$\begin{cases} n_j = \dfrac{2\rho_i}{\Delta x} \qquad \rho_i = R\cos\eta_i \\ \eta_{ij} = \dfrac{2\eta_i}{n_j} \end{cases} \tag{12}$$

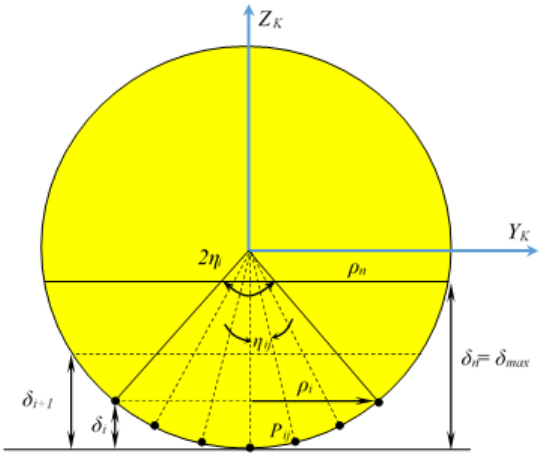

Fig. 3. Discretization of the roller in the contact region to check if the burnishing tool is within workpiece region.

Where Δx is the length of each grid in workpiece. Once the η_{ij} is determined, the position of each point in the roller coordinate system can be identified:

$$\begin{bmatrix} X^K_{P_{ij}} \\ Y^K_{P_{ij}} \\ Z^K_{P_{ij}} \end{bmatrix} = \begin{bmatrix} R \\ r\sin\eta_{ij} \\ -r\cos\eta_{ij} \end{bmatrix} \tag{13}$$

For the time t, the coordinate of the transformed point of the roller from the local coordinate system to the workpiece coordinate system i.e. (X^W_P, Y^W_P) is checked with the X_{max} and Y_{max} in H matrix. This point is accepted if the transformed point is within the workpiece range.

e) Checking the coincidence: For each transformed point (X^W_P, Y^W_P), a coincidence limit compared to workpiece gridding points i.e. H (X, Y) is defined where the distance between the points is less than ε. In other words, if the distance of (X^W_P, Y^W_P) and H (X, Y) is less than ε, the coincidence condition is met. In the present work, the coincidence limit has been set to ε=0.01µm.

f) Checking the engagement: For the coincident points, the values of $Z_P{}^W$ are compared with the Z in H matrix. If the $Z_P{}^W$ is less than Z, in the H matrix, the Z is replaced by $Z_P{}^W$; otherwise, the Z is kept.

g) 3D surface topography: When the process is finished (i.e., t=t_{max}), the updated workpiece matrix determines the final surface topography.

Experiments

In the present investigation, the stainless steel 316 L blocks with dimensions of 70 mm in length, 30 mm in width, and 10 mm in thickness were built by laser powder bed fusion process. An EOS M280 3D printer machine with 1100 nm wavelength discontinuous Yb-fibre laser was used to manufacture samples. The volumetric energy density for fabrication was set on 100 J/mm^3.The samples were printed based on optimized standard EOS parameters with 195W laser power, 1083 mm/s scan speed, 90 µm hatch spacing, and 20 µm layer thickness. As-built samples were detached from a substrate using wire electrical discharge machining.

A multi-roller rotary burnishing process was utilized for post-processing as-printed samples. The commercial burnishing tool model SPF20-S20 manufactured by SUNGINO cooperation comprises four rollers made of hardened steel. The length and diameter of rollers are 10 mm and 4 mm, respectively. During each revolution of the tool, a width of 20 mm can be burnished by this

tool. Thus, its more efficient in the vibration of flat surfaces compared to a single roller (or ball) burnishing tool. Fig. 4 demonstrates the experimental setup.

The main characteristic that needs to be measured in the present study is surface topography and roughness. In order to do so, a 3D surface roughness machine, namely TylorHobson was utilized. Measurements were carried out in a 1 mm^2 squared area.

The experiment was planned for confirmation of the developed model. For the SLM process mentioned in section 3.1, the sample was built based on the standard EOS parameter used for 3D printing of stainless steel 316. Then, the obtained surface topography and roughness of until material were compared with the predicted values.

For the burnishing process, from our preliminary experiments and the developed model, it was found that the main burnishing factor that has the greatest influence on the surface roughness evolution of the SLM sample is the burnishing depth. Thus, in the present study, the burnishing experiments for processing as-built material were carried out by variation of burnishing depth at 0.05 mm and 0.075 mm and 0.1 mm, while the spindle speed and linear velocity were kept constant at 800 RPM and 200 mm/min.

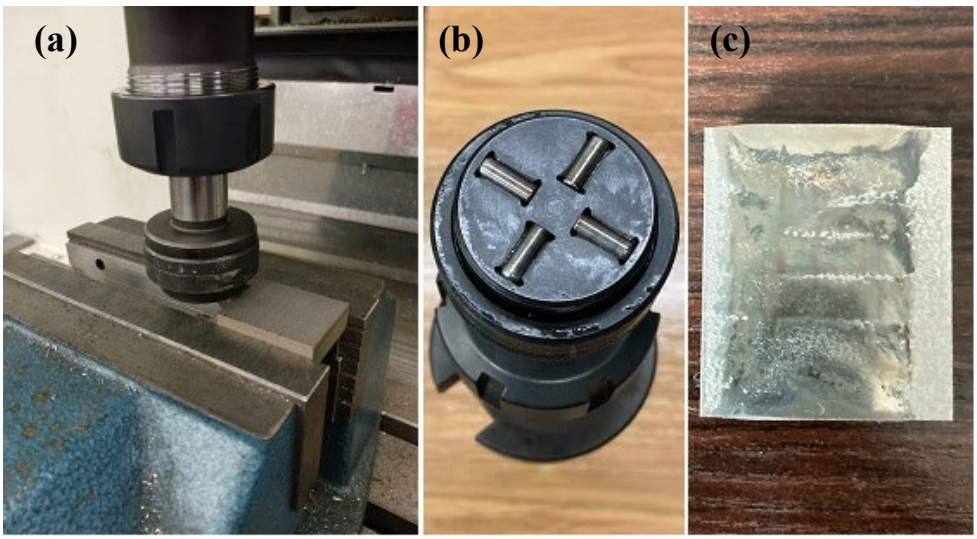

Fig. 4. (a) Burnishing experimental setup (b) multi-roller burnishing tool (c) burnished sample.

Results and Discussion

Fig. 5 illustrates the comparison between the measured and predicted surface roughness (Ra) of different samples. According to the presented results, it is seen that they are in good agreement in general; it indicates that the developed evolutionary simulation is reliable. It is seen that the maximum distance from the peak and valley (Rt) for as-built material measured through surface roughness is 12.303, while the predicted value is 12.276 µm. Moreover, the arithmetic surface roughness (Ra) value for the SLMed sample measured by the experiment was 6.62 µm, while the simulated value is 7.10 µm. For the burnished sample with depth of 0.05mm, the surface peaks are flattened due to plastic deformation. The Rt value was measured at 6.595 µm while the predicted one was at 7.353 µm. Fig. 5 illustrates that the arithmetic surface roughness values which were obtained through experiments and simulation are 2.65 µm and 3.23 µm, respectively. Moreover, for the samples processed by 0.075 mm and 0.1 mm burnishing depth, the measured values of Rt are 4.943 and 2.818, respectively. The Rt values obtained by the simulation model for the same processing conditions are 4.852 and 2.45, respectively. Also, the arithmetic surface roughness value which was measured by experiments are 1.11 µm and 0.288 µm, respectively. On the other

hand, the predicted values of Ra, which the simulation model calculated, are 1.31 µm and 0.355 µm, respectively.

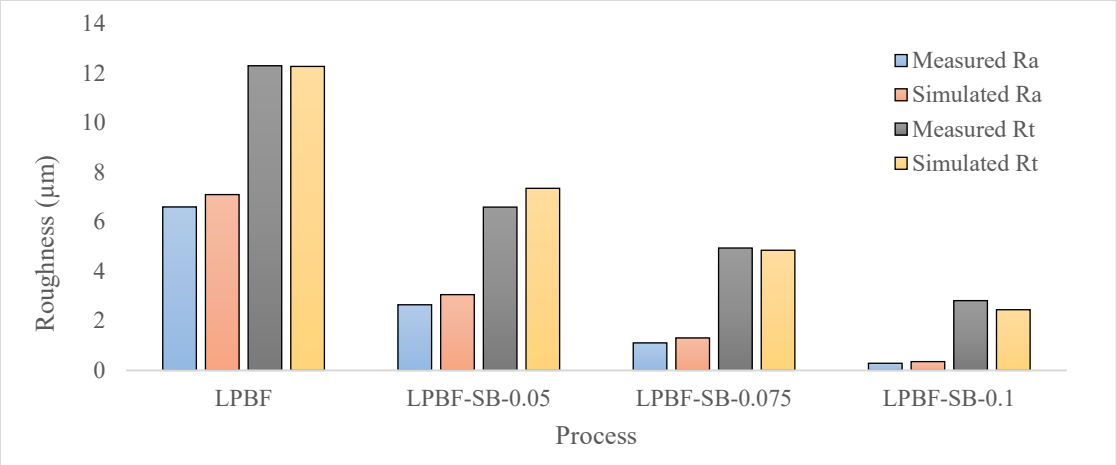

Fig. 5. Comparison between measured and predicted values of Ra and Rt under different conditions.

Fig. 6 shows that there are consistencies between the measured and predicted surface topography of the samples. In all the samples its seen that sinusoidal behaviour exist in one direction and the variation of surface peaks and valleys are following same trends while the burnishing depth increases.

Summary

The obtained results can be summarized as follows:

- The surface roughness of SLMed sample fabricated at EOS standard setting were in close agreement with those derived from the simulation model. The prediction error for calculating the Ra and Rt were about 7.5% and 2%, respectively.
- It was found that the prediction error of the surface roughness increases as burnishing is applied as a sequential process. Also, the error values increase by increasing the burnishing depth. However, the maximum prediction error in the worst case is 18.8% for Ra and 12.8% for Rt. This difference can be attributed to fracture of agglomerated partially fused particles because of high degree of plastic deformation resulting in big scratches on the surface of burnished sample during experiment; which hasn't been included in the model.

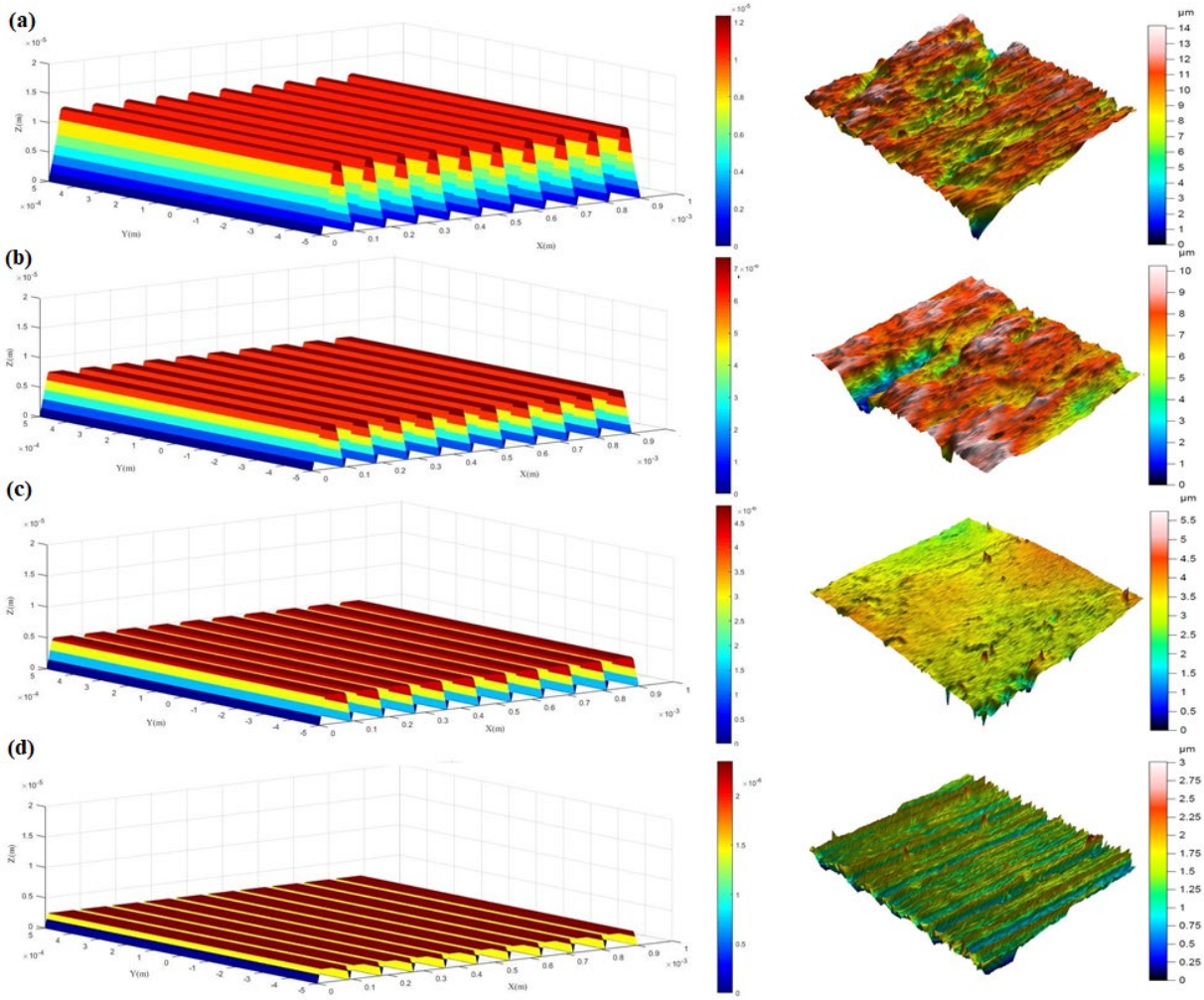

Fig. 6. Comparison of measured and simulated 3D surface topography (a) As-built (b) burnishing depth of 0.05 mm (c) burnishing depth of 0.075 mm (d) burnishing depth of 0.1 mm.

References

[1] J. Bedmar, N. Abu-ward, S. García-Rodríguez, B. Torres, J. Rams, Influence of the surface state on the corrosion behaviour of the 316 L stainless steel manufactured by laser powder bed fusion, Corros. Sci. 207 (2022) 110550. https://doi.org/10.1016/j.corsci.2022.110550

[2] L. Chen, B. Richter, X. Zhang, K.B. Bertsch, D.J. Thoma, F.E. Pfefferkorn, Effect of laser polishing on the microstructure and mechanical properties of stainless steel 316L fabricated by laser powder bed fusion, Mater. Sci. Eng. A 802 (2021) 140579. https://doi.org/10.1016/j.msea.2020.140579

[3] S. Bagehorn, J. Wehr, H.J. Maier, Application of mechanical surface finishing processes for roughness reduction and fatigue improvement of additively manufactured Ti-6Al-4V parts, Int. J. Fatigue 102 (2017) 135-142. https://doi.org/10.1016/j.ijfatigue.2017.05.008

[4] H. Zhang, R. Chiang, H. Qin, Z. Ren, X. Hou, D. Lin, G.L. Doll, V.K. Vasudevan, Y. Dong, C. Ye, The effects of ultrasonic nanocrystal surface modification on the fatigue performance of 3D-printed Ti64, Int. J. Fatigue 103 (2017) 136-146. https://doi.org/10.1016/j.ijfatigue.2017.05.019

[5] H. Soyama, Y. Okura, The use of various peening methods to improve the fatigue strength of titanium alloy Ti6Al4V manufactured by electron beam melting, AIMS Mater. Sci. 5 (2018) 1000-1015. https://doi.org/10.3934/matersci.2018.5.1000

[6] H. Soyama, C. Kuji, Improving effects of cavitation peening, using a pulsed laser or a cavitating jet, and shot peening on the fatigue properties of additively manufactured titanium alloy Ti6Al4V, Surf. Coat. Tech. (2022) 129047. https://doi.org/10.1016/j.surfcoat.2022.129047
[7] X.L. Yuan, Y.W. Sun, L.S. Gao, S.L. Jiang, Effect of roller burnishing process parameters on the surface roughness and microhardness for TA2 alloy, Int. J. Adv. Manuf. Technol. 85 (2016) 1373-1383. https://doi.org/10.1007/s00170-015-8031-0
[8] G. Rotella, L. Filice, F. Micari, Improving surface integrity of additively manufactured GP1 stainless steel by roller burnishing, CIRP Annals, 69 (2020) 513-516.
[9] S. Sunny, R. Mathews, H. Yu, A. Malik, Effects of microstructure and inherent stress on residual stress induced during powder bed fusion with roller burnishing, Int. J. Mech. Sci. 219 (2022) 107092. https://doi.org/10.1016/j.ijmecsci.2022.107092
[10] R.K. Raaj, P.V. Anirudh, C. Karunakaran, C. Kannan, A. Jahagirdar, S. Joshi, A.S.S. Balan, Exploring grinding and burnishing as surface post-treatment options for electron beam additive manufactured Alloy 718, Surf. Coat. Tech. 397 (2020) 126063. https://doi.org/10.1016/j.surfcoat.2020.126063
[11] A.C. de Bruijn, G. Gómez-Gras, M.A. Pérez, On the effect upon the surface finish and mechanical performance of ball burnishing process on fused filament fabricated parts, Additive Manufacturing 46 (2021) 102133. https://doi.org/10.1016/j.addma.2021.102133
[12] J. Ning, E. Mirkoohi, Y. Dong, D.E. Sievers, H. Garmestani, S.Y. Liang, Analytical modeling of 3D temperature distribution in selective laser melting of Ti-6Al-4V considering part boundary conditions, J. Manuf. Process. 44 (2019) 319-326. https://doi.org/10.1016/j.jmapro.2019.06.013
[13] B. Liu, G. Fang, L. Lei, An analytical model for rapid predicting molten pool geometry of selective laser melting (SLM), Appl. Math. Model. 92 (2021) 505-524. https://doi.org/10.1016/j.apm.2020.11.027
[14] H.Q. Chen, Q.H. Wang, Modelling and simulation of surface topography machined by peripheral milling considering tool radial runout and axial drift, Proceedings of the Institution of Mechanical Engineers, Part B: Journal of Engineering Manufacture 233 (2019) 2227-2240. https://doi.org/10.1177/0954405419838384